

REPORT DOCUMENTATION PAGE

Form Approved
OMB No. 0704-0188

The public reporting burden for this collection of information is estimated to average 1 hour per response, including the time for reviewing instructions, searching existing data sources, gathering and maintaining the data needed, and completing and reviewing the collection of information. Send comments regarding this burden estimate or any other aspect of this collection of information, including suggestions for reducing the burden, to Department of Defense, Washington Headquarters Services, Directorate for Information Operations and Reports (0704-0188), 1215 Jefferson Davis Highway, Suite 1204, Arlington, VA 22202-4302. Respondents should be aware that notwithstanding any other provision of law, no person shall be subject to any penalty for failing to comply with a collection of information if it does not display a currently valid OMB control number.

PLEASE DO NOT RETURN YOUR FORM TO THE ABOVE ADDRESS.

1. REPORT DATE (DD-MM-YYYY) 18-04-2005		2. REPORT TYPE Final Technical		3. DATES COVERED (From - To) Nov. 2002 -- Jan. 2005	
4. TITLE AND SUBTITLE Numerical Studies of Low Grazing Angle Microwave Scattering from Breaking Water Waves				5a. CONTRACT NUMBER	
				5b. GRANT NUMBER N00014-03-1-0134	
				5c. PROGRAM ELEMENT NUMBER	
6. AUTHOR(S) James C. West				5d. PROJECT NUMBER	
				5e. TASK NUMBER	
				5f. WORK UNIT NUMBER	
7. PERFORMING ORGANIZATION NAME(S) AND ADDRESS(ES) Oklahoma State University Electrical and Computer Engineering 202 ES Stillwater, OK 74078				8. PERFORMING ORGANIZATION REPORT NUMBER	
9. SPONSORING/MONITORING AGENCY NAME(S) AND ADDRESS(ES) Office of Naval Research Ballston Centre Tower One, Code 334 800 N. Quincy Street Arlington, VA 22217-5660				10. SPONSOR/MONITOR'S ACRONYM(S) ONR	
				11. SPONSOR/MONITOR'S REPORT NUMBER(S)	
12. DISTRIBUTION/AVAILABILITY STATEMENT APPROVED FOR PUBLIC RELEASE					
13. SUPPLEMENTARY NOTES					
14. ABSTRACT The microwave backscattering from breaking water waves at small illumination grazing angles (LGA) has been investigated using computational electromagnetics (CEM) techniques. Good agreement is achieved between the numerically calculated and experimentally measured backscattering from a wave tank plunging breaker. The large measured HH/VV polarization ratio is due to the shape of the wave crest and the multi-path scattering from the wave crest and front face. The HH/VV ratio is maintained when the wave crest has modified nonuniformities in azimuth, although it is affected by larger variations. The two-scale model fails to predict the LGA scattering from a 3-D gently spilling breaker even after the steepest wave features have been removed.					
15. SUBJECT TERMS Sea surface EM scattering Rough surface EM scattering Computational electromagnetics					
16. SECURITY CLASSIFICATION OF:			17. LIMITATION OF ABSTRACT	18. NUMBER OF PAGES	19a. NAME OF RESPONSIBLE PERSON
a. REPORT	b. ABSTRACT	c. THIS PAGE			James C. West
U	U	U	UU	19	19b. TELEPHONE NUMBER (Include area code) (405) 744-6096

Numerical Studies of Low Grazing Angle Microwave Scattering from Breaking Water Waves

James C. West
Principal Investigator
ONR Contract N00014-03-1-0134

Project period: 1 November 2002 – 31 January 2005

1 Introduction

Research efforts have been performed to facilitate the understanding and efficient modeling of microwave scattering from steep and reentrant features on the sea surface at low grazing angle (LGA) illumination. LGA sea surface scattering is characterized by brief bursts of power known as "sea spikes". Sea spikes are often characterized by horizontally polarized transmit/received (HH) power exceeding that at vertical polarization (VV) by more than 10 dB (Lewis and Olin, 1980; Trizna, 1991). (Events where HH exceeds VV are sometimes also referred to as "super events".) This behavior is not predicted by traditional rough surface scattering models such as the Kirchhoff approximation (KA) or two-scale model (TSM) that have proven useful at moderate incidence. Sea spikes have been correlated with breaking waves in experimental studies in both laboratory wave tanks and the open sea (Kalmykov and Pustovoytenko, 1976; Lee *et al.*, 1995; Smith *et al.*, 1996; Lee *et al.*, 1999; Fuchs *et al.*, 1999), with maximum responses occurring at or near the time of maximum steepness of the breaking wave. Previously, the most successful models to explain sea spike responses use fairly simple optical approaches to describe the multipath scattering from the breaking crest (Wetzel, 1986; Trizna, 1997). The differing multipath responses at the two polarizations give differing interference, leading to the sea spike. In previous work, we incorporated the effects of the wave crest shape and of roughness on the face of the breaker into two-dimensional electromagnetic scattering models that demonstrated a single-scattering source of super events (West, 2002). The goal of this project was to fully validate these two-dimensional models through direct comparison of modeled scattering with wave-tank experimental results, and to apply advanced numerical scattering algorithms to more complicated general three-dimensional wave cases to model additional scattering mechanisms that are not evident in two-dimensional studies.

2 Approach

Electromagnetic scattering models are usually formulated using approximations to Maxwell's equations that allow the derivations of closed form solutions, but also limit the range of applicability to specific surface conditions. The rough sea surface is quite complicated, with features ranging from quite small to quite large compared to the electromagnetic wavelength. It is therefore impossible to characterize the scattering with a single, universal scattering model. Instead, the approach considered in this work is to treat specific scattering mechanisms with unique models that are formulated for that particular case. The "global" model is formed by combining the effects of the individual models in a physically consistent manner. The three primary mechanisms considered are quasi-specular reflection from steep wave crests, distributed-surface scattering from random roughness on

the crest, and multipath reflection between the crest and other points on the surface. The validity of the models under specific conditions was tested through comparison with reference scattering found using computationally expensive numerical methods. Where appropriate, existing models are extended to yield more accurate results as more realistic surface profiles are considered. As the results are only as valid as the underlying surface representations used in the calculations, the work is focused on directly measured profiles of breaking waves when possible, or on numerically generated surfaces that are thought to provide realistic representations of the dominant scattering features.

The project was divided into two distinct, but related, efforts. The first was the application of a numerical scattering algorithm to a series of measured wave profiles measured in a wave tank by James Duncan of the University of Maryland under ONR funding. Plunging breaker waves were mechanically generated in the University of Maryland wave tank. The time evolution of the upwind/downwind cross-section of the breaking crest was continuously measured by a video camera mounted to an instrument carriage that traveled with the wave crest. A laser sheet illuminated a fluorescent dye within the water to provide a signal in the video stream that was digitally detected to yield the wave profile. The full measurement technique was shown in Duncan *et al.* (1999). A numerical electromagnetics code was applied to the detected wave profiles at Oklahoma State, giving a time history of the wave radar cross-sections. Simultaneous radar measurement of the backscattering was performed by Mark Sletten of the Naval Research Laboratory (NRL), also under ONR funding. The simultaneous experimental radar measurements provide ground truth to which the numerical results may be compared to fully validate the technique of applying the numerical scattering routines to measured waves. Refinements over previous, similar experimental efforts included movement of the antennas farther from the wave crest to ensure that they were operating in the far field, as well as improved optical measurement of both the cavity under the jet and the region in front of the crest. Infrared (IR) photographs of the wave crests (taken by Jeff Smith of the Naval Research Laboratory under ONR funding) were also made during the breaking stage, revealing the azimuthal variation of the post-breaking wave that cannot be measured by the planar laser sheet. The NRL measurements are described in Sletten *et al.* (2004).

The scattering from the measured wave-tank crests was numerically found using a hybrid technique that extends the moment method (MM) using the geometrical theory of diffraction (GTD) (West *et al.*, 1998). MM/GTD is a two-dimensional computational method that assumes the wave profile is ideally uniform in the azimuthal direction, making it well suited for application to the measured upwave/downwave cross-sectional wave-tank wave profiles. The technique allows the modeled scattering surface to be numerically extended to infinity with little additional computational overhead, thereby eliminating the artificial edge diffraction from truncated surface edges that can affect the scattering calculations. This in turn allows either ideal uniform plane wave illumination or realistic antenna patterns to be used in the scattering studies, giving a realistic representation of the contributions of different wave features to the total scattering cross-section. Impedance boundary conditions are applied to the surface to represent the finite conductivity of water at microwave frequencies. This technique has been used extensively by the PI in previous wave scattering studies (West *et al.*, 1998; West and Sletten, 1997; West, 2000, 2002).

The second major effort of the project was to characterize the scattering from fully three dimensional wave crests (that is, waves that are not uniform in one dimension). Direct application of standard numerical electromagnetic algorithms to general three-dimensional scattering problems is far more computationally expensive than the previously performed two-dimensional studies. The scattering calculations were therefore performed using an accelerated multilevel fast multipole algorithm (MLFMA) that was implemented in house (Zhao and West, 2005b). This technique is derived to treat general scattering target geometries, so it is ideally suited to application to the reentrant features associated with breaking water waves. In this particular implementation, resistive loading of the edges of the modeled surface is used to reduce the surface currents to very small values, thereby suppressing the edge diffraction that would lead to inaccurate scattering cross-sections. Plane wave illumination can again be used to give realistic illumination of the scattering features. The finite

conductivity of the surface is treated using impedance boundary conditions. The iterative solution of the MLFMA system is performed using the generalized minimum residual (GMRES) algorithm in conjunction with a thresholded incomplete LU decomposition (ILUT) preconditioner. The preconditioner reduces the number of GMRES iterations needed for convergence from greater than 100 to approximately 15 in most cases. The validity of the MLFMA technique was confirmed through comparison of the scattering from simple 3-D shapes with analytical and 2-D based numerical results. The technique is fully described in Zhao and West (2005b).

One difficulty in performing the three-dimensional scattering studies is that directly measured 3-D wave profiles are not readily available. Instead, we have relied upon synthesizing 3-D crests from existing numerically generated or measured 2-D crest profiles. The synthesis process allows the complexity of the wave target to be carefully controlled, with new scattering features methodically introduced. The relative contribution of each feature type can therefore be identified, and approaches to accurately predict the backscattering without numerically solving the full 3-D problem may be formulated and tested. 3-D test plunging breaker crests were generated from the numerically generated LONGTANK profiles (Wang *et al.*, 1995) that represent the time evolution of an intermediate scale (approximately 1 m wavelength) plunging breaker. These profiles have been used extensively in 2-D electromagnetic scattering studies (Holliday *et al.*, 1998; West, 2002; Kim and Johnson, 2002), and have become a standard test case for LGA multipath scattering from breaking waves. Additionally, a sample 3-D spilling breaker crest was synthesized by azimuthally aligning the 2-D upwave/downwave cross-sections of a gently spilling breaker measured in the University of Maryland wave tank.

3 Results

3.1 Wave Tank Results

Fig. 1 shows the time history of the plunging breaker crest measured in the University of Maryland wave tank. The individual two-dimensional surface profiles measured in the upwave/downwave plane at the center of the wave tank are stacked vertically. The vertical dimension therefore shows the evolution of the wave with increasing time. Since the instrument carriage that carried the optical measurement system was moving with the crest of the wave, features that appear to move to the left in the figure with increasing time are moving faster than the wave crest, while features that move to the right are moving slower than the crest. The wave steepens and a jet forms from 0 to 150 ms. The jet impacts the surface at approximately 150 ms, after which there is “splash-up” response from 200 ms to 400 ms. After that, turbulent cells continuously form on the crest that are left behind as the wave propagates.

Fig. 2 shows the geometry used in the numerical calculations of the backscattering from the measured crests. Additional optical measurements performed by the University of Maryland showed that the surface displacement returned slowly to zero the region in front of the wave. A spline interpolation was therefore used to join the front of the measured crest to a zero-displacement point placed approximately 1.25 m in front of the crest. The surface was then smoothly joined to infinite extensions that were angled at 30° to horizontal. This angle extension allows the use of the hybrid 2-D MM/GTD numerical method. The complete modeled surface with the extensions is shown in Fig. 2. The large dot in Fig. 2 shows the approximate phase-center of the wide-band horn antenna used in the Naval Research Laboratory measurements. The dotted line shows the multiple back-reflection paths from the crest to the antennas with the front face extension. The illumination grazing angle at the wave peak is approximately 6° (the incidence angle is 84°). Measured antenna patterns provided by the manufacturer were manually digitized and included in the numerical calculations. Antenna beamwidths were at least 20° at the frequencies considered, so the features were approximately uniformly illuminated.

Fig. 3 shows a comparison between the 7 GHz scattering measured by the NRL radar and that

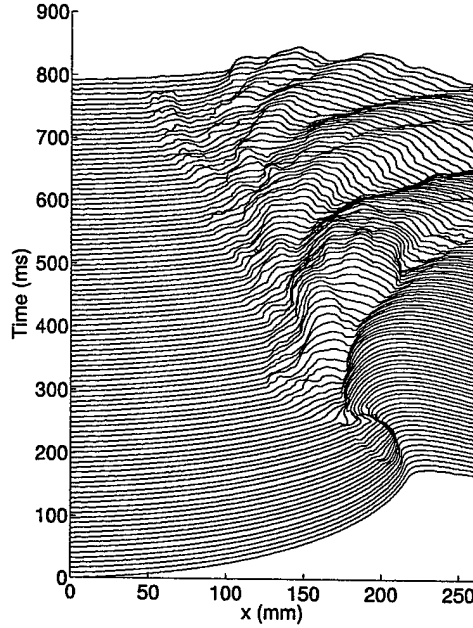


Figure 1: Time history of the upwave/downwave cross-section of a plunging breaker wave crest optically measured in a wave tank.

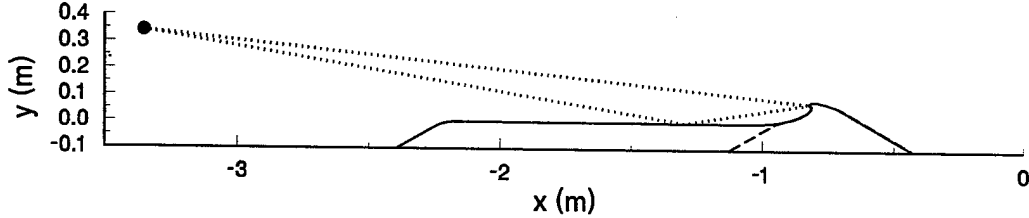


Figure 2: Extensions of a single 2-D measured crests used in 2-D MM/GTD backscattering calculations. The dashed line shows the extension used to avoid multipath reflection. The solid line shows the front face extension used to give multipath reflection. The dotted line shows multipath reflections when the antenna is placed at the dot.

found numerically. The absolute levels of the radar cross-sections should not be directly compared since the measurements yield a true 3-D cross-section in dB relative to 1 m^2 , while the 2-D numerical results yield 2-D cross-sections in dB relative to 1 m . The cross-sections show the classic sea-spike super-event response with HH backscattering exceeding VV by up to 25 dB. Overall excellent agreement is obtained during the jetting and splash-up stages of breaking from 0 to 400 ms. In particular, the HH backscattering rises rapidly during the jetting stage in both, with the maximum reached just after 100 ms. HH backscattering drops quickly after that, but then rises again during the splash-up with a second relative maximum appearing just before 400 ms. VV backscattering on the other hand remains very low for the first 100 ms, after which it rises quickly to 200 ms. After that the level oscillates, but the mean VV level remains approximately constant through 400 ms in both cases. After 400 ms the agreement is not as good. At HH polarization this is due in large part to the noise floor of the radar measurements, which appears at -18 dB-m^2 . However, it is clear the HH backscattering drops dramatically after the splash-up region, which is consistent with numerical calculations. The measured VV backscatter decreases slowly after 400 ms. The numerical VV cross-

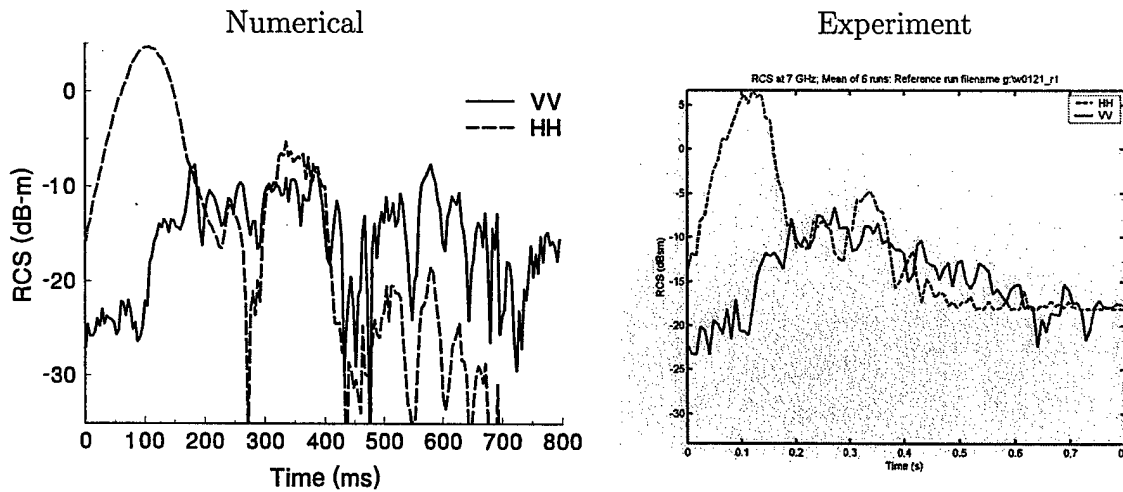


Figure 3: Comparison of numerical and experimental 7 GHz backscattering from the wave tank breaker of Fig. 1.

sections also show a general downward trend during this time, but oscillates much more rapidly. The IR measurements showed that the surface becomes very nonuniform in the azimuthal direction during this time. This is not reflected in the 2-D cross-sectional measurements, and therefore not in the numerical scattering calculations.

Fig. 4 shows a wideband comparison (6 GHz to 12 GHz) of the NRL experimental results and the numerical calculations. Overall the agreement is good. The VV backscattering has a major response centered at 11 GHz/50 ms in both, with broader strong signals during at lower frequency from 100 ms to 400 ms. HH response is dominated by the strong response during the jetting at 100 ms at all frequencies, with weaker responses at 375 ms.

Fig. 5 shows the dependence of the Doppler shift found at 7 GHz as a function of time. (The Doppler shifts are centered at 0 Hz since the frame of reference moved with the wave crest.) HH polarization again shows excellent agreement, with the jetting dominating and a later weaker response during the splash-up. The jetting response is centered at approximately 15 Hz since the jet moves faster than the wave phase velocity. The VV Doppler response shows weak responses extending out to 40 Hz during the jetting around 200 ms. Stronger response occurs at 0 Hz/200 ms. After that, the dominant responses increase in frequency, reaching 20 Hz at 350 ms. After 400 ms the agreement is somewhat poorer, again due the azimuthal non-uniformity of the wave in this time period. However, significant Doppler signals appear from -20 Hz to +20 Hz in both the experimental and numerical scattering throughout this time.

As a final test, the numerical scattering from the measured wave crests was found without the front face extensions that give the multipath back-reflection. An example of the resulting surface is shown as the dashed line in Fig. 1. The time history of the numerically found backscattering from this wave history is shown in Fig. 6. The VV backscattering is only slightly changed from the corresponding numerical results in Fig. 3. This confirms that multipath reflection at vertical polarization is damped due to the Brewster angle effects of the finite conductivity sea water. The initial low level of the VV backscattering is due to the shape of the crest features themselves, with back reflections from the convex jet and concave cavity regions destructively interfering. At horizontal polarization, however, the backscattering during jetting has dropped dramatically, confirming that the strong cross-sections observed are in part due to the multipath. Therefore, both the crest-feature and multipath effects contribute to the experimentally observed strong super event.

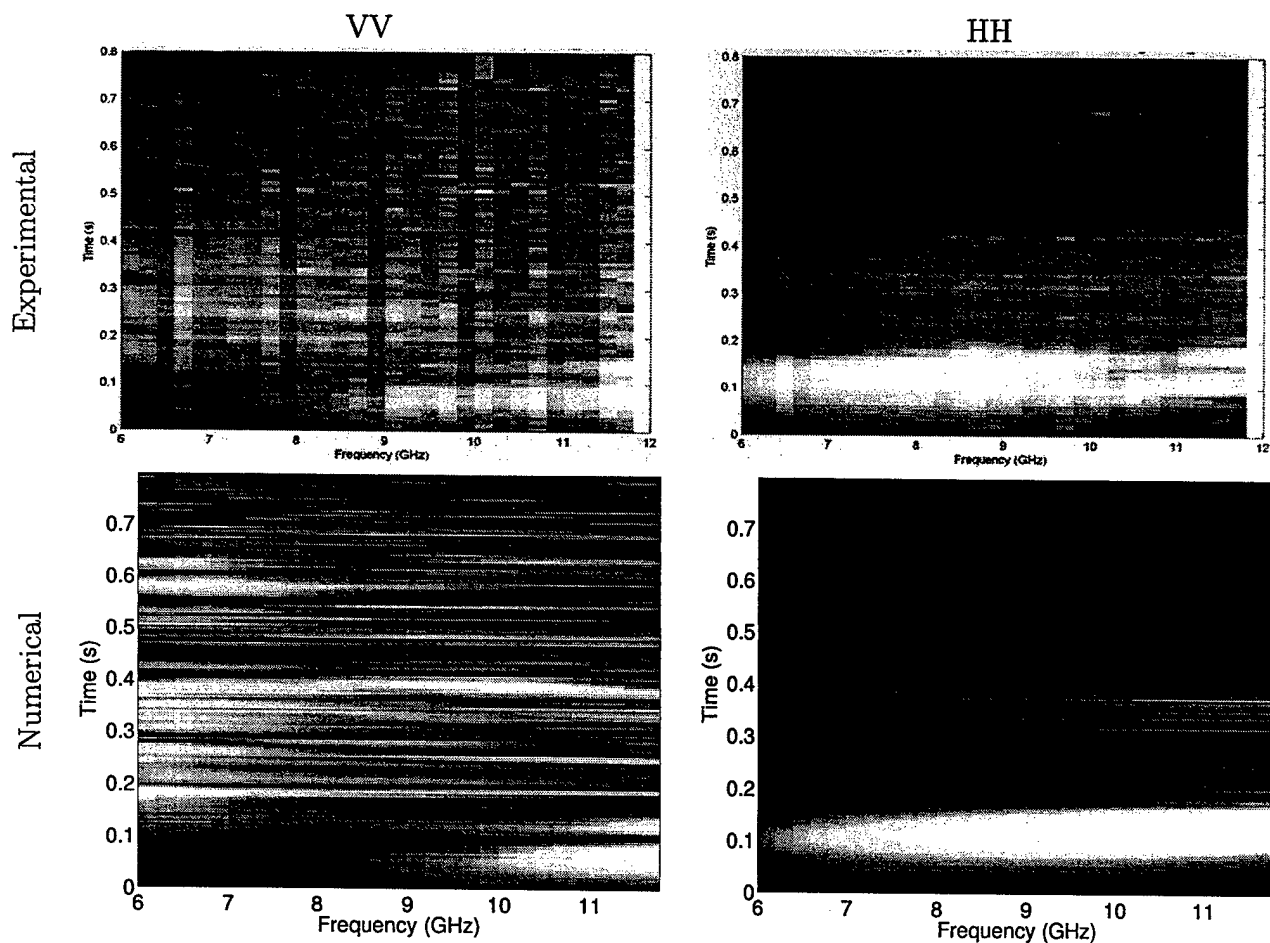


Figure 4: Wideband comparison of the backscattering from the breaker of Fig. 1. The upper plots are the experimental results and the lower are numerical. Axes are time (s) versus frequency (GHz).

3.2 3-D Plunging Crest Results

All 3-D calculations shown were performed at 10 GHz using the MLFMA scattering code described above.

3.2.1 Uniform jets

Fig. 7 shows the 2-D LONGTANK wave crests that were used to synthesize the plunging-breaker 3-D test surfaces. A 3-D crest synthesized from LONGTANK waves 1 through 13 is shown in Fig. 8a. The profile was formed by aligning the crests of the LONGTANK waves in the cross-wave direction, with wave 13 in the center. Profiles 12 to 1 were then placed on both sides sequentially, with the spacing between the profiles decreasing as the distance moved from the center. Spline interpolation in the cross-wave direction gave a continuous surface in this range. Profile 1 was also repeated over 6 cm at the extreme edge to give a region for the resistive loading needed to avoid edge diffraction. The leading and trailing edges of the waves were also extended by 9 cm for the resistive loading.

The backscattering from the wave crest of Fig. 8 when looking directly upwave is shown in Fig. 9. The HH backscattering found using the MLFMA numerical routine exceeds that at VV at nearly

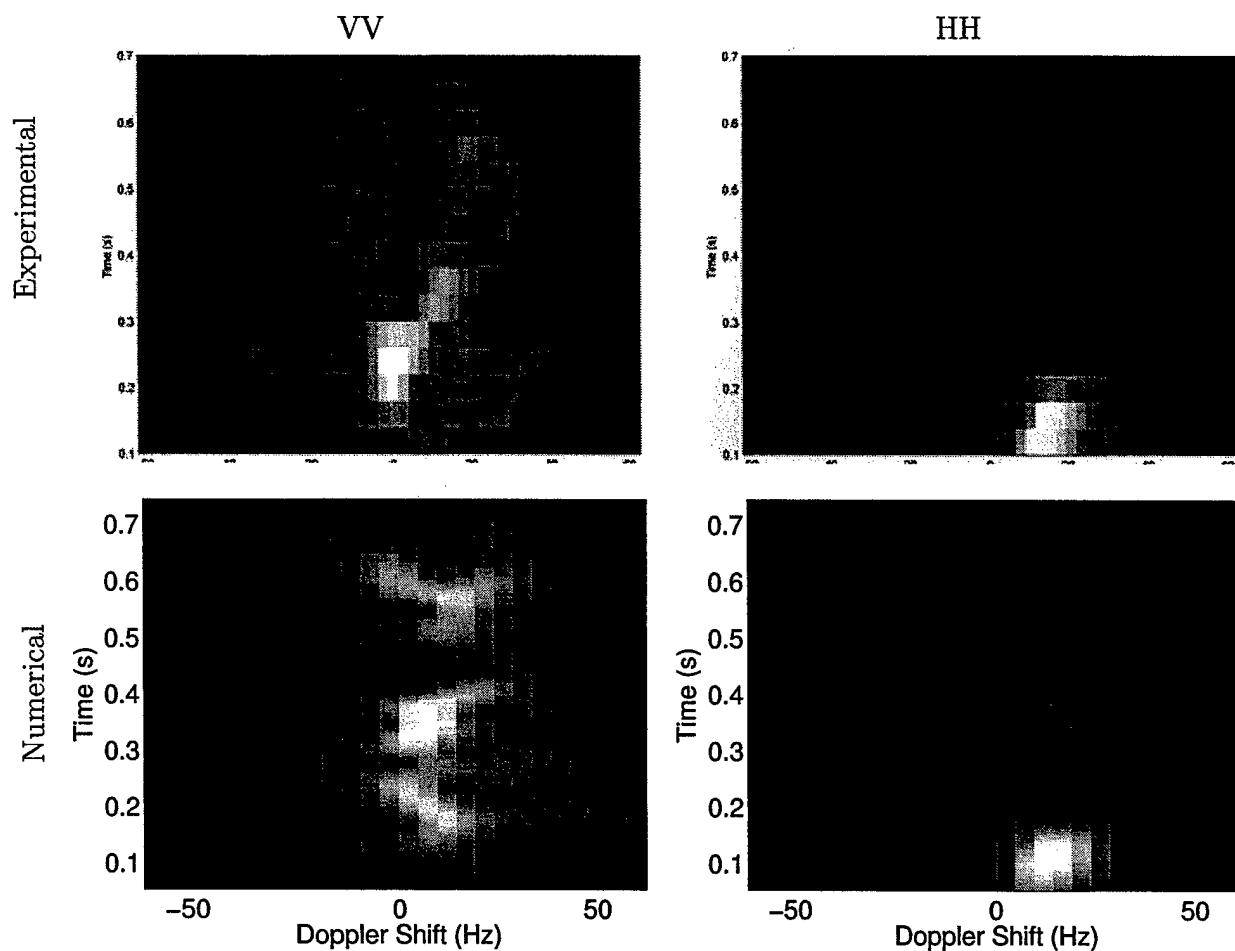


Figure 5: Comparison of Doppler shifts of 7 GHz backscattering from the plunging breaker of Fig. 1. The axes are time (s) versus Doppler shift (Hz).

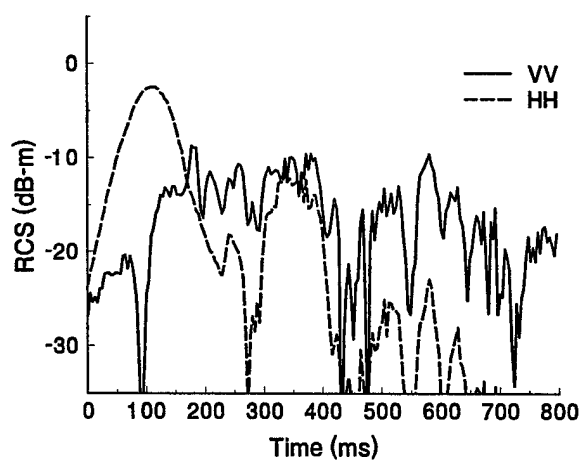


Figure 6: Numerical 7 GHz backscattering from measured wave crests with no front face extension.

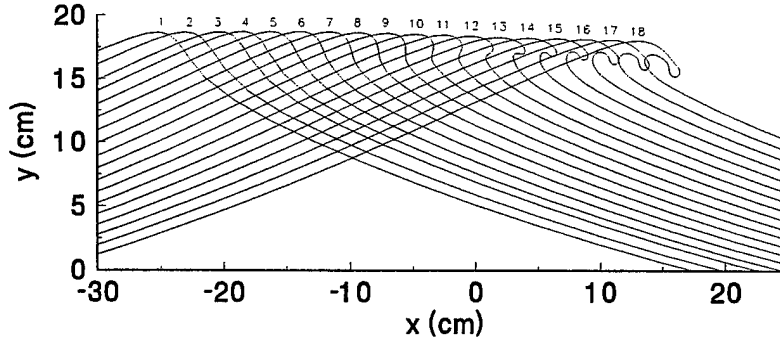


Figure 7: LONGTANK waves used to synthesize 3-D wave crests.

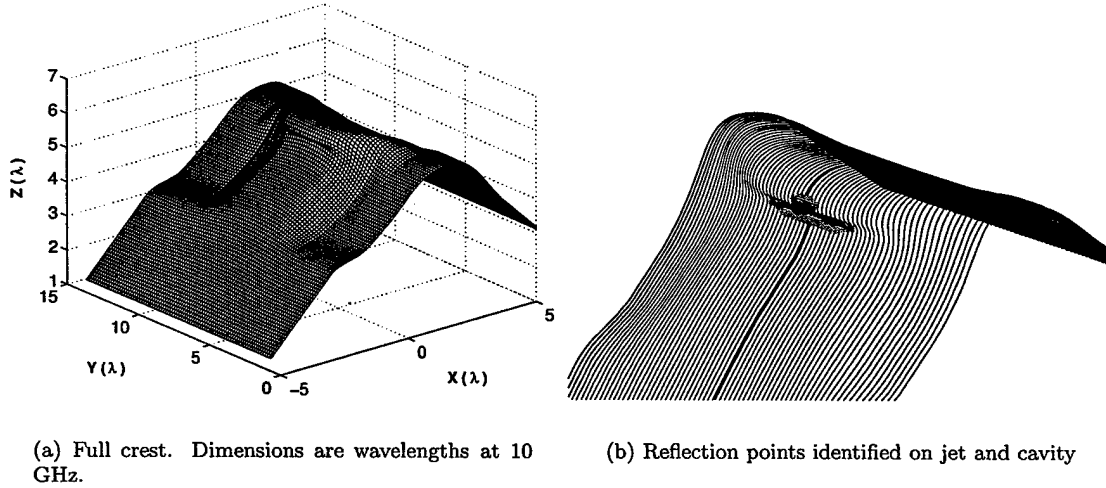


Figure 8: 3-D wave crest synthesized from LONGTANK waves 1 through 13.

all incidence angles. A strong null occurs in the VV backscattering at 75° incident (15° grazing). This behavior is consistent with that observed previously with 2-D wave profiles, and appears as the small VV cross-sections during jetting in Fig. 3. The VV null in the 2-D backscattering was shown to be due to interference in the back-reflection from specular points on the wave on the forming jet and within the cavity below the jet. The corresponding reflection points for the 3-D wave are shown in Fig. 8b. The radius of curvature of the surface at the reflection points is smaller than the electromagnetic wavelength, so the reflection from these points differs at the two polarizations. This was modeled in the 2-D case by multiplying the reflection from each point predicted by geometrical optics by the correction factor

$$M = \begin{cases} 1 + j \frac{11}{16(ka)} - \frac{353}{512(ka)^2} & \text{VV,} \\ 1 - j \frac{5}{16(ka)} + \frac{127}{512(ka)^2} & \text{HH,} \end{cases} \quad (1)$$

where k is the electromagnetic wave number, a is the radius of curvature at the reflection point, and j is the square root of -1. This "extended" geometrical optics (EGO) introduces opposite phase shifts to the reflected fields at VV and HH, giving destructive interference at VV and constructive interference at HH. Fig. 3 also shows the EGO prediction of the backscattered field when applied

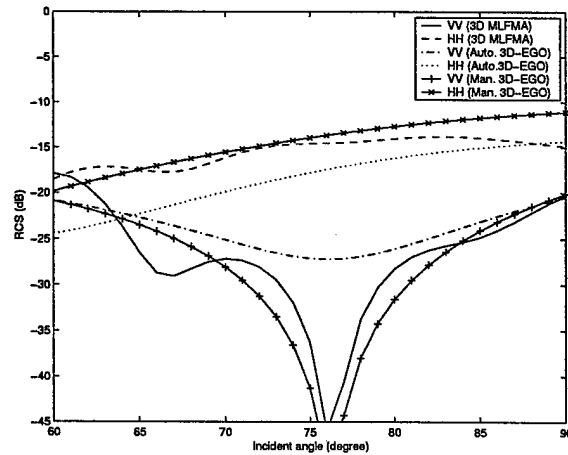


Figure 9: 10 GHz backscattering from the crest of Fig. 8. Shown are the scattering cross-sections found using MLFMA and the 3-D extended geometrical optics. Axes are radar cross-section (dB) versus incidence angle ($^{\circ}$).

to the reflection points of Fig. 8b. The correction factor was applied to the surface curvature at the reflection points in both the upwave/downwave and crosswave directions. A direct application of EGO to the reflection points found by an automatic procedure gave a reasonable prediction of the HH/VV ratio overall, but manual adjustment of the surface radii of curvature at the reflection points was needed to fully represent the deep null in the VV backscattering. A fully automated method of predicting the deep VV null from the wave properties at the reflection points was not found.

Fig. 10 shows the dependence of the backscattering from the crest of Fig. 8a on azimuth angle. 0° indicates directly upwave illumination. The high HH/VV ratio seen in Fig. 9 is maintained out 8° azimuth, beyond which the VV backscattering increases. Fig. 11 shows the reflection points on the wave crest at 5° and 10° azimuth. At 5° , reflection points occur both on the jet of the wave and in the cavity, giving destructive interference between the concave and convex point reflection. At 10° however the reflection points have moved off the main part of the wave onto the side, and the concave cavity region is not well defined at the reflection point.

Fig. 12 shows a 3-D wave crest formed from LONGTANK waves 1 through 15. This wave has a much more developed jet. At 0° azimuth the cavity is fully shadowed from the incident illumination by the jet so there is no concave reflection point. This is reflected in the backscattering shown in Fig. 13. No VV cancellation appears at 0° azimuth. However, as the azimuth angle increases to 5° a deep VV null appears. This is explained by the reflection points identified at 5° azimuth shown in Fig. 12. As the azimuth angle increases, the cavity underneath the jet becomes visible, giving the concave reflection point needed for the VV cancellation. Overall, we have consistently observed VV cancellation whenever there are both concave and convex back-reflection points directly illuminated when the radii of curvature at the reflection points are on the order of one half the electromagnetic wavelength.

3.2.2 Non-uniform jets

Additional tests were performed to determine the effect of jet non-uniformities on the backscattering. Fig. 14 shows three profiles formed from LONGTANK waves 1 through 13 with ripples of increasing magnitude introduced into the waves. The 0° azimuth backscattering from these waves is shown in part d of the figure. The backscattering is very similar to that in Fig. 9 when small and moderate

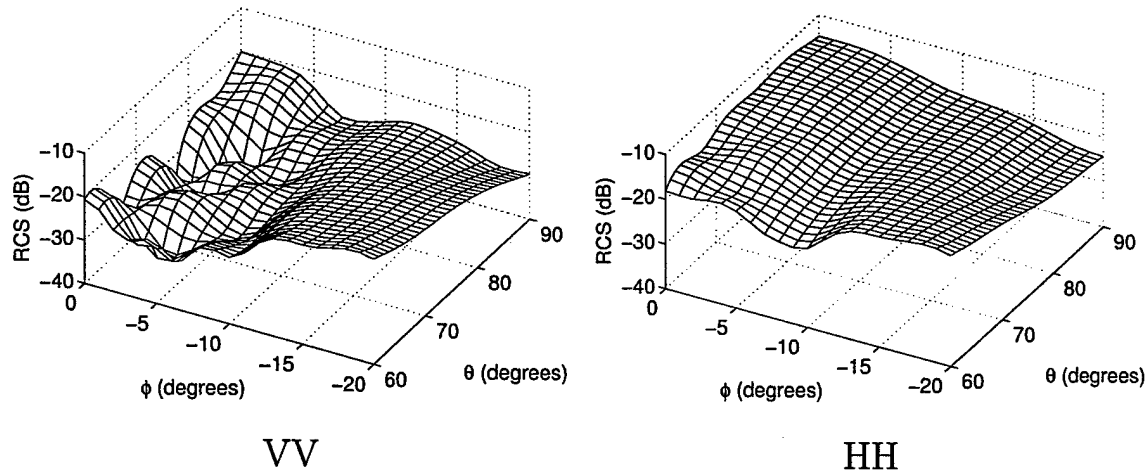


Figure 10: Dependence of backscattering from crest of Fig. 8 on azimuth. ϕ is the azimuthal angle (referenced to directly upwave looking) and θ is the incidence angle.

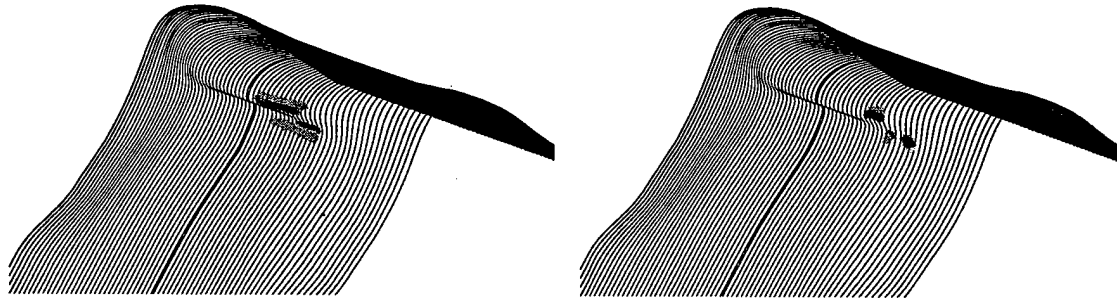


Figure 11: Back reflection points on wave of Fig. 8 at 5° and 10° azimuth.

roughness is introduced. However, with the largest roughness HH drops in magnitude by as much as 7 dB, and the VV null is much shallower. Fig. 15 repeats the calculations with wave crests formed from LONGTANK waves 1 through 18, giving a much more developed jet. With small and moderate jet roughness HH exceeds VV by up to 10 dB at all but the largest incidence (smallest grazing). However, with the largest roughness the HH backscattering suddenly becomes very low, with a very deep null at 74° incidence (16° grazing). This is the first time behavior such as this has been observed for any wave profile. Efforts are currently underway to explain this response.

3.2.3 Modeling of non-uniform jets

Fig. 16 demonstrates the efforts underway to develop a technique to model the backscattering from surfaces with non-uniform jets without the need to numerically find the backscattering from the full 3-D surface. In this, the scattering from the individual crest features are isolated by directly treating smaller sub-surfaces. Part c) of the figure shows a crest that was formed from LONGTANK waves 1 through 13 with moderate jet roughness. The surface was formed so there are three jet maxima of the same type, and two jet minima. Back-reflection points were identified on both the jet and the cavity region at the jet maximum, and in the cavity region at the jet minima. The back-reflection from the jet maxima regions were found by applying the MLFMA code to the surface shown in Fig. 16 a), which included only a single jet maxima. The MLFMA code was then applied to the surface in part b) of the figure that included two jet maxima and one minimum. Coherently subtracting

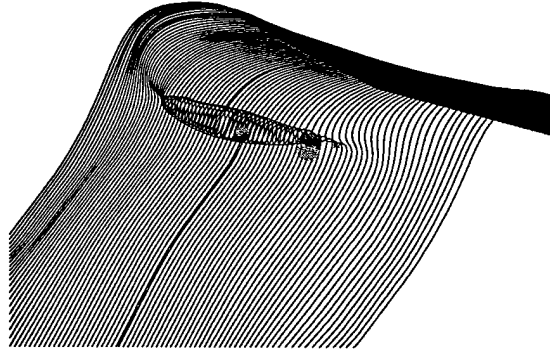


Figure 12: 3-D wave crest formed from LONGTANK waves 1 through 15. Shown are the back reflection points at 5° azimuth.

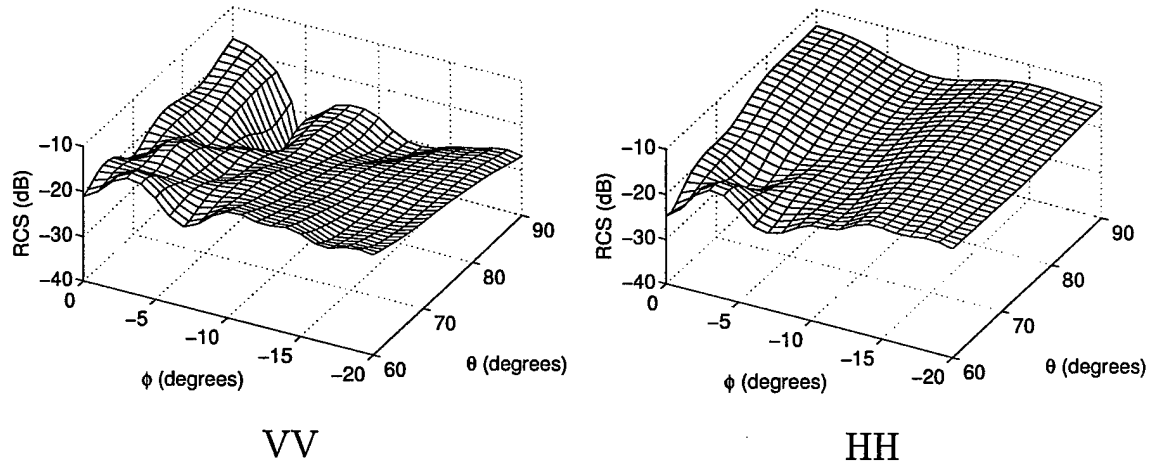


Figure 13: Dependence of backscattering from crest of Fig. 12 on azimuth.

twice the field scattered from the part a) surface from the field scattered from the part b) surface scattered field yielded the backscattered field associated only with the cavity reflection at the jet minima. All reflection points are then characterized. Finally, the backscattered field from the full surface in part c) of Fig. 16 was modeled by the coherent addition of the fields associated with the isolated reflection points. The comparison with the direct MLFMA results for the complete surface are shown in Fig. 16 d). Excellent agreement is achieved.

Fig. 17 performs an analysis similar to that of Fig. 16, but with the wave crest formed from LONGTANK waves 1 through 16 and the final surface (part c)) consisting of three jets. In this case, the coherent combination of the fields associated with the jet maxima and minima (as isolated from the surfaces in parts a) and b) of the figure) is effective in predicting the VV field scattered from the three-jet surface of part c). At HH polarization, however, the coherent addition severely underpredicts the reference MLFMA field at all incidence angles above 70° . Multiple interactions between the jet features therefore affect the backscattered field at this polarization.

As shown by the test cases, the approach of coherently combining the fields scattered from individual jet features should be applicable to any 3-D wave profile where the reflection points are well defined and multiple scattering is limited. The advantage of this approach is that it may be used with extremely large surfaces that cannot be completely modeled using MLFMA. The much smaller sub-surfaces can be considered individually, and their scattered fields combined appropriately to

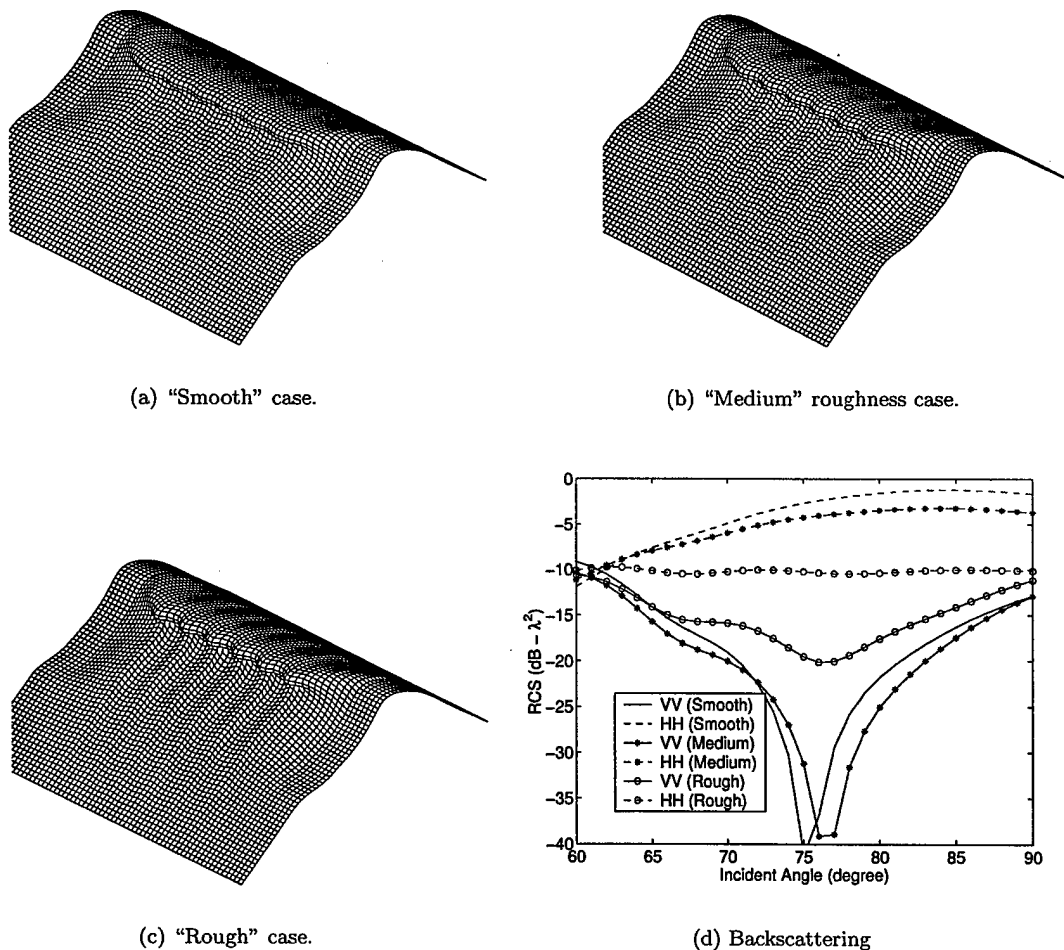


Figure 14: 0° azimuth backscattering from crests formed from LONGTANK waves 1 through 13. Parts a) through c) show the increasing roughness of jet regions used. The surface widths are approximately 14λ . Part d) shows the MLFMA calculated backscattering.

model the full surface. The primary disadvantage is that the technique will break down when there are large features that give multiple scattering. The surface cannot be modeled as isolated reflecting points in this case.

A final test case with more random, very large crest roughness is shown in Fig. 18. LONGTANK waves 1 through 18 were used to form this surface. This surface yields VV backscattering exceeding HH at all angles considered, despite the fact that the individual LONGTANK waves that yield significant scattering individually give HH greater than VV. It appears that interference between the various backscattering features leads to this result, although the exact cause has not yet been identified.

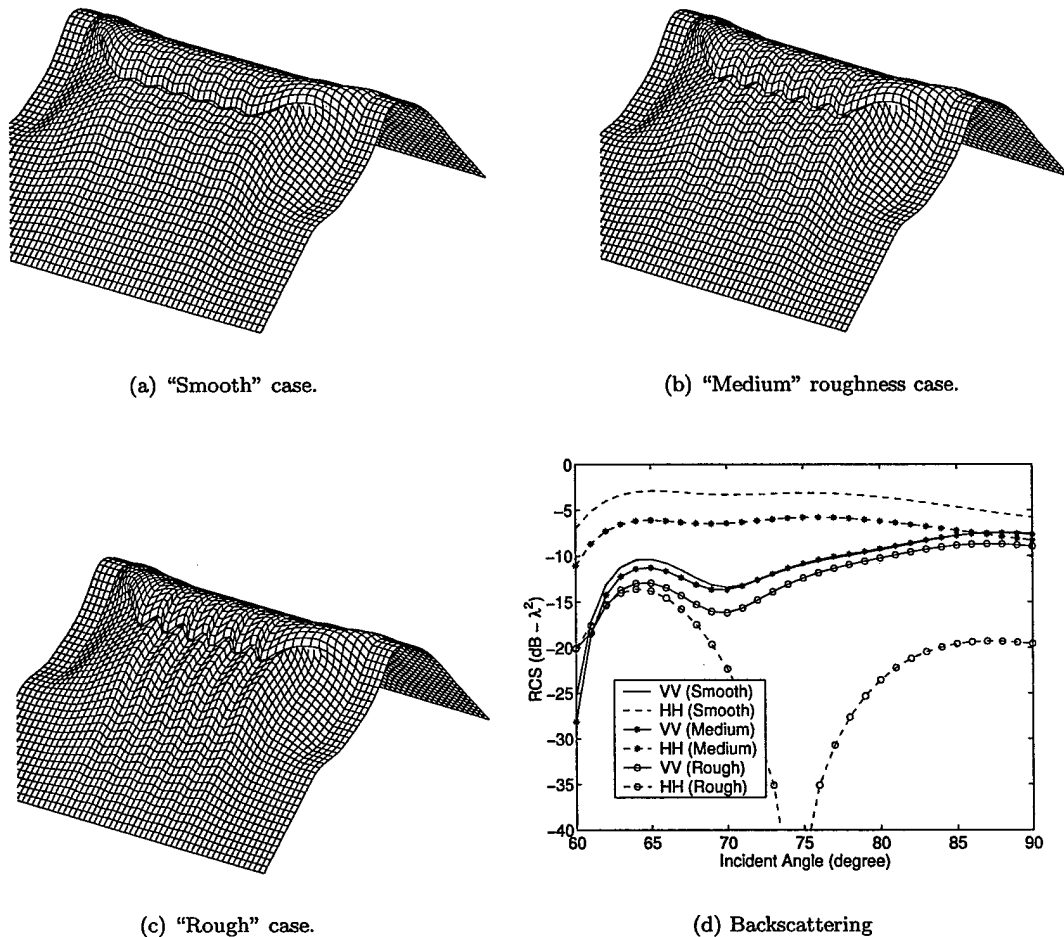


Figure 15: Same as Fig. 14, but with the crest formed from LONGTANK waves 1 through 18. The surface widths are approximately 17.5λ .

3.3 3-D Spilling Breaker Crest

Another mechanism that can lead to microwave backscattering from breaking water waves is distributed surface scattering from the turbulent “scar” that remains on the surface after breaking. The standard model to predict distributed-surface scattering is the two-scale model, which first separates the roughness into large- and small-scale components through filtering. The Kirchhoff approximation model is then applied to the large-scale roughness and the small-perturbation model is applied to the small-scale component, and the results combined either coherently or incoherently (depending upon whether a deterministic or stochastic analysis is being performed) to yield the composite scattering. In previous work (West and Ja, 2002), the two-scale model was applied to the individual 2-D profiles of Fig. 19, giving a model-based prediction of the time history of the scattering from the evolving wave crest. Comparison with reference scattering found using the 2-D MM/GTD approach showed that the two-scale model gave a credible estimate of the overall scattering magnitude at 80 degree incidence at times after the steepest features on the surface had subsided, although it was

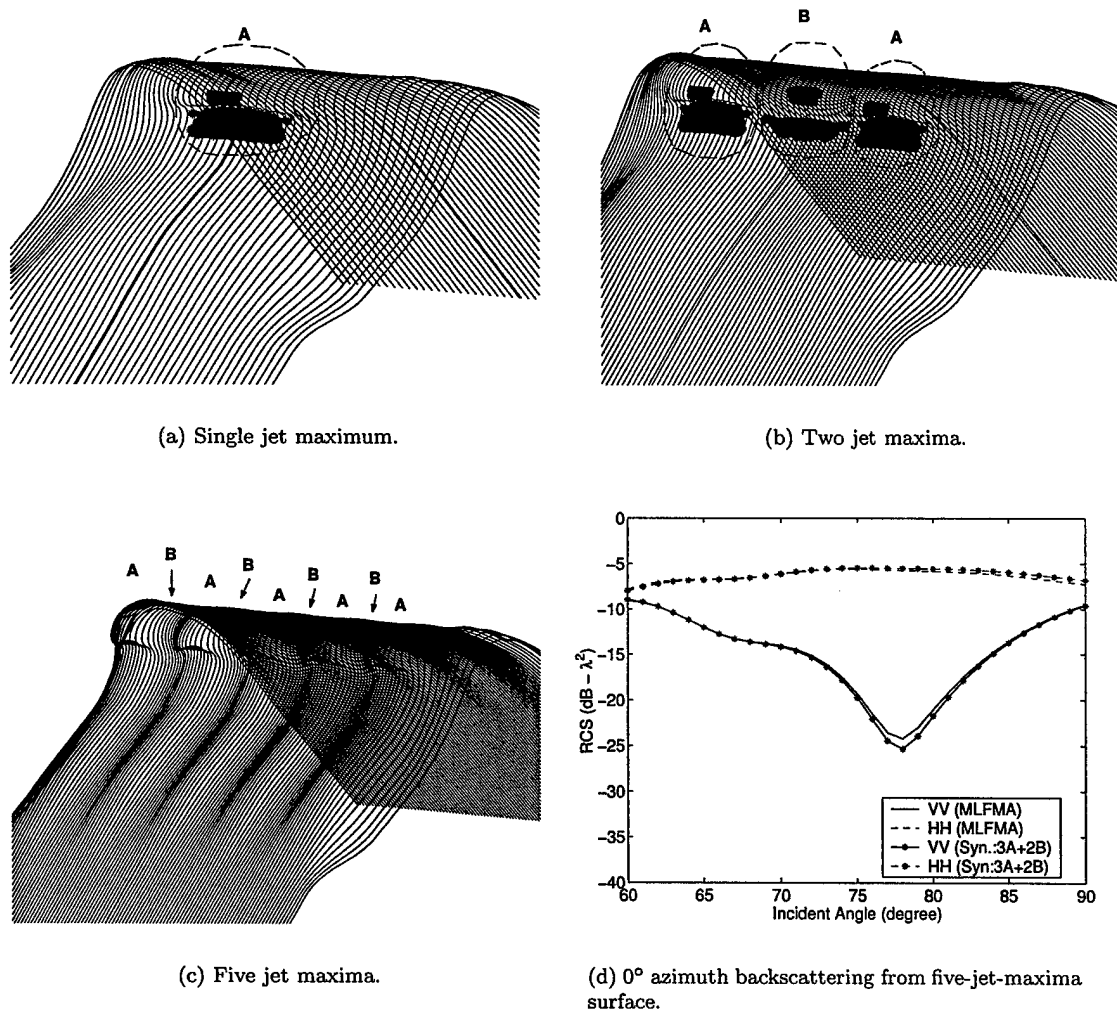


Figure 16: Crests formed from LONGTANK waves 1 through 12 with moderate jet roughness and calculated backscattering..

noticeably less accurate than at moderate incidence (45 degrees). Here the analysis extended to the 3-D electromagnetic problem (surfaces that are rough in two dimensions).

The first 3-D surface to be considered was shown in Fig. 20a. This surface was formed by azimuthally aligning all profiles of Fig. 19, including those with the steepest features centered at 300 ms. MLFMA was used to find the reference scattering from the surface. Resistive loading 3λ in length was applied to the leading and trailing edges of the surface, and 2λ in width on the azimuthal edges, where λ is the electromagnetic wavelength. The two-scale model was applied by first applying multiple passes of a triangularly weighted window to the surface in both the range and azimuthal directions to filter out the small-scale roughness and leave the large-scale surface. The large-scale roughness was then subtracted from the original surface to yield the small-scale roughness. The number of passes of the moving average was varied to yield different cutoff wave numbers in the scale-separation filter. The two-scale model was then deterministically applied to the separated roughness (taking into account the finite conductivity of sea water) to yield a radar

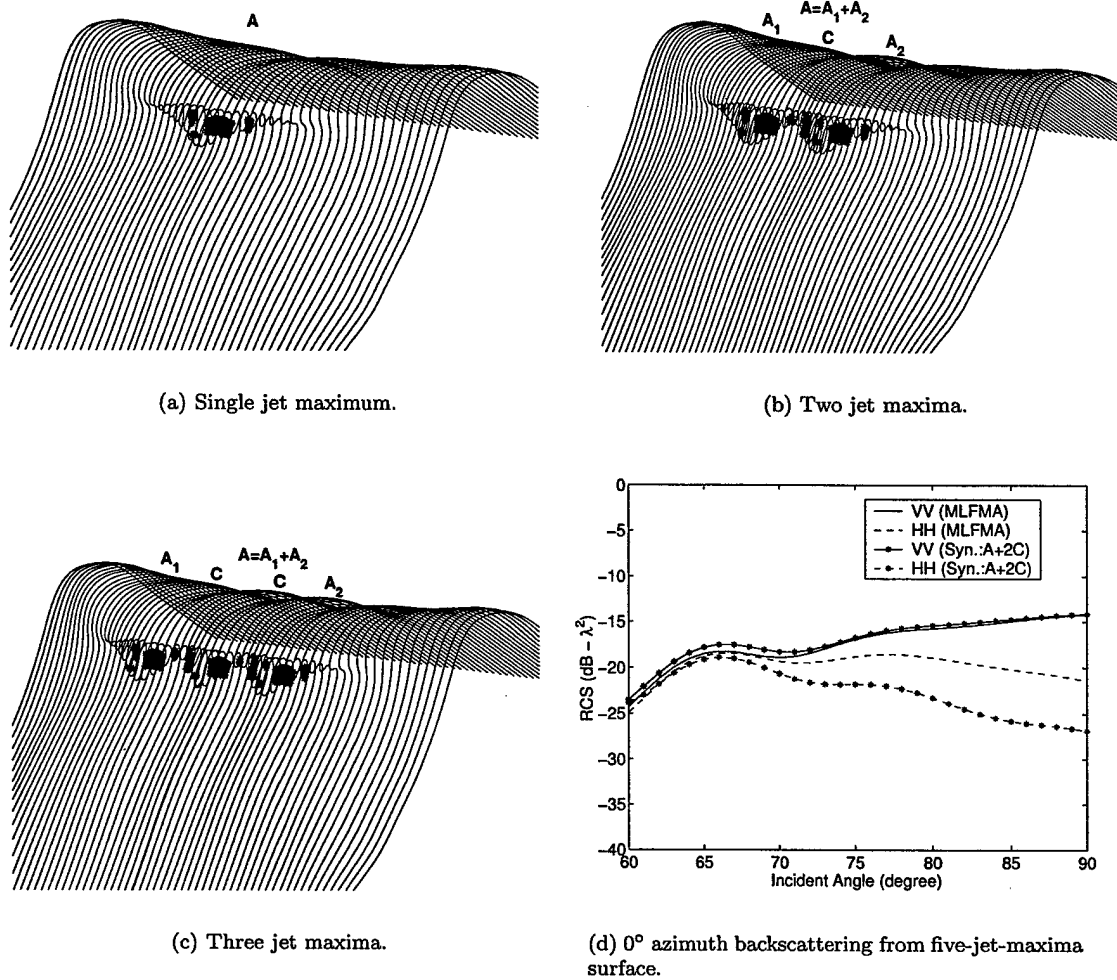


Figure 17: Crests formed from LONGTANK waves 1 through 16 with large jet roughness and calculated backscattering.

cross-section that could be directly compared to the reference MLFMA cross-sections.

The two-scale model scattering with three different scale-separation cutoff wave numbers (K_T) from the surface of Fig. 20a is compared with the corresponding MLFMA scattering in Fig. 21. The cutoff was changed by a factor of two between the figures. The incidence angles shown are limited to the small grazing (large incidence) region of interest. The two-scale model underpredicts the HH backscattering at all incidence angles and TSM cutoff wave numbers. At VV, TSM overpredicts the scattering at thresholds of $K_T = k/1.4$ and $K_T = k/1.0$. Raising the threshold to $K/0.7$ decreases the TSM scattering, but the oscillations in the MLFMA scattering are not predicted and errors approaching 5 dB occur. $K_T = k/0.7$ also yields the poorest agreement at HH, and in fact no threshold could be found that consistently yielded good agreement at both polarizations. This behavior is not unexpected considering the very steep 2-D profiles near 300 ms in Fig. 19 were included in the 3-D surface. The 2-D two-scale model was inaccurate in this case, so similar inaccuracies appear in this initial 3-D case. To address this problem, a modified surface was formed from the post-breaking profiles of Fig. 19 (after 424 ms), thereby eliminating the steepest sections.

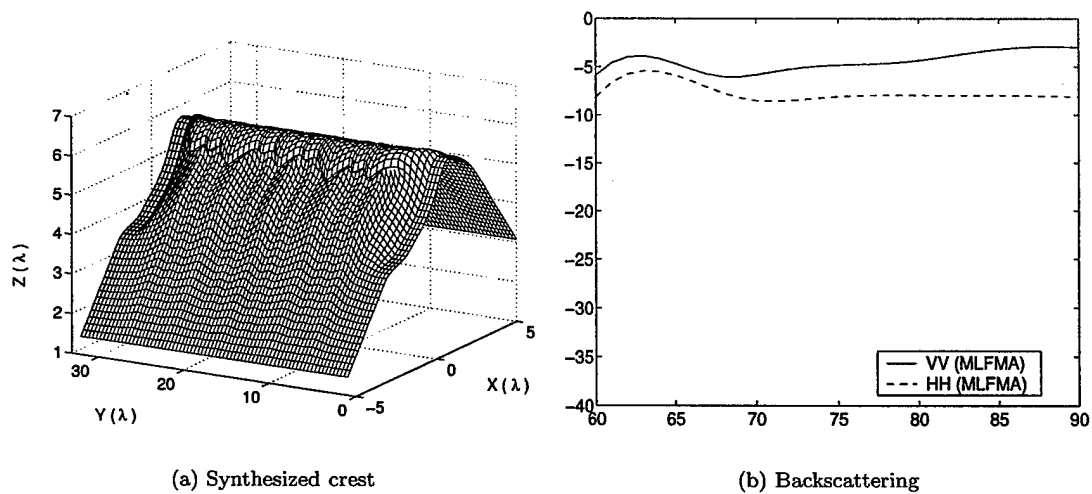


Figure 18: Backscattering from a crest formed from LONGTANK wave 1 through 18 with a random jetting structure. a) Crest with a very rough jet formed from LONGTANK waves 1 through 18. b) The MLFMA 10 GHz backscattering at 0° azimuth.

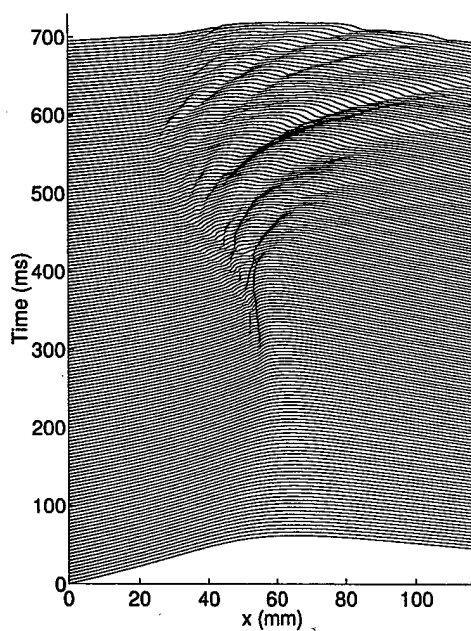


Figure 19: Measured time history of the upwind/downwind cross-section of a gently spilling breaker.

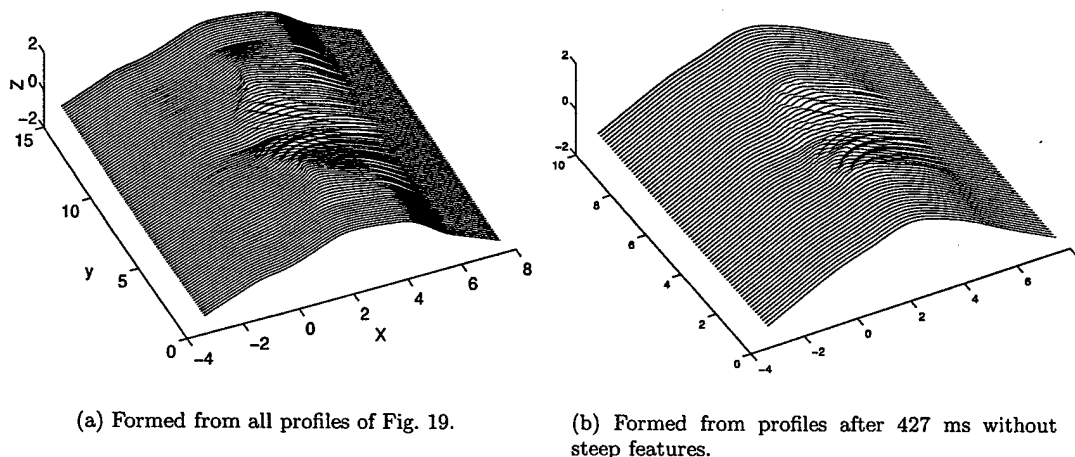


Figure 20: Three-dimensional crests synthesized from 2-D crest measurements of Fig. 19.

The resulting profile (termed the “post-breaking profile”) is shown in Fig. 20b. The corresponding two-scale analysis over a factor of 2 change in the scale-separation wave number is shown in Figures 14 and 15. The two-scale model proves much less sensitive to the scale separation in this case, and gives excellent results at both polarizations with thresholds of $K_T = k/1.4$ and $K_T = k/2.0$ below 73° grazing. This improved accuracy is due to the lack of steep features on the wave. A full analysis of the TSM scattering from the 3-D spilling breaker waves is given in Zhao and West (2005a).

Overall, the accuracy of the two-scale model when applied to the 3-D post-breaking surface is similar to that of the 2-D two-scale model when applied to the individual post-breaking problems. It therefore potentially can be used to provide rough estimates of the distributed-surface scattering from wave crests down to about 70° . However, the small section of steep crest in Fig. 20a made TSM highly inaccurate and dependent upon the scale-separation threshold used. This indicates that this small steep section is a very strong (nearly dominant) contributor to the overall scattering from the spilling breaker, and questions the usefulness of TSM at low grazing illumination even with weakest of breaking waves.

References

- DUNCAN, J. H., QIAO, H., PHILOMIN, V., and WENZ, A., 1999, Gentle spilling breakers: Crest profile evolution. *J. Fluid Mech.*, **379**, 191–222.
- FUCHS, J., REGAS, D., WASEDA, T., WELCH, S., and TULIN, M. P., 1999, Correlation of hydrodynamic features with LGA radar backscatter from breaking waves. *IEEE Trans. Geosci. Remote Sens.*, **37**, 2442–2460.
- HOLLIDAY, D., DERAAD, L. L., and ST-CYR, G. J., 1998, Sea spike backscatter from a steepening wave. *IEEE Trans. Antennas Propagat.*, **46**, 108–113.
- KALMYKOV, A. I. and PUSTOVOYTENKO, V. V., 1976, On polarization features of radio signals scattered from the sea surface at small grazing angles. *J. Geophys. Res.*, **81**, 1960–1964.
- KIM, H. and JOHNSON, J. T., 2002, Radar image study of simulated breaking waves. *IEEE Trans. Geosci. Remote Sens.*, **40**, 2143–2150.

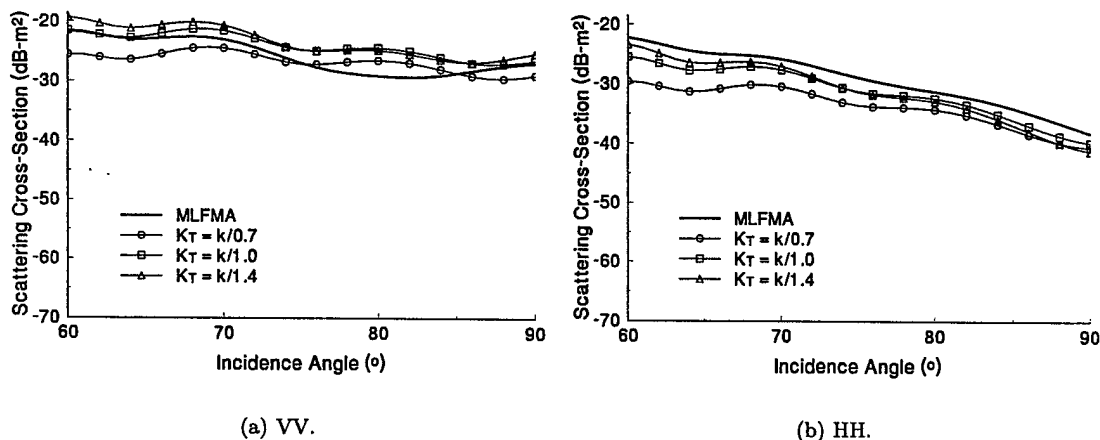


Figure 21: Backscattering from spilling breaker surface of Fig. 20a.

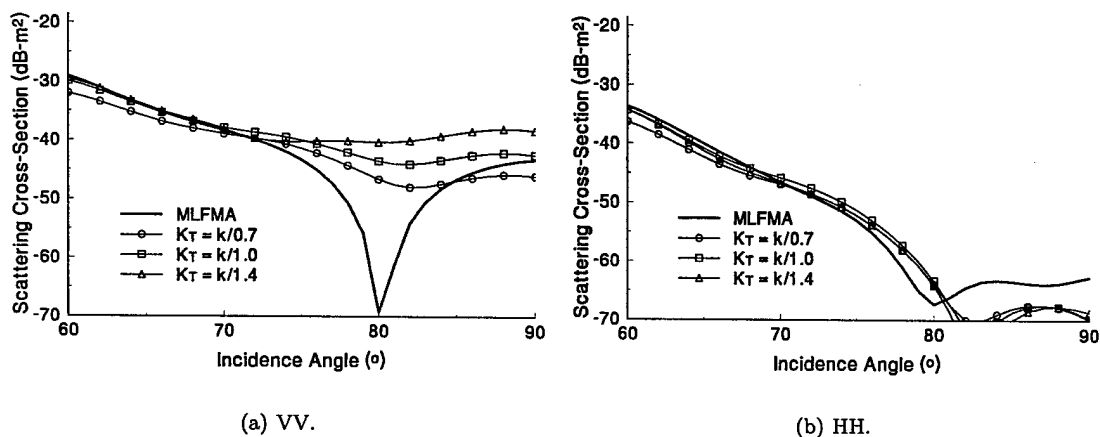


Figure 22: Backscattering from spilling breaker surface of Fig. 20a.

- LEE, P. H. Y., BARTER, J. D., BEACH, K. L., HINDMAN, C. L., LAKE, B. M., RUNGALDIER, H., SHELTON, J. C., WILLIAMS, A. B., YEE, R., and YUEN, H. C., 1995, X band microwave backscattering from ocean waves. *J. Geophys. Res.*, **100**, 2591–2611.
- LEE, P. H. Y., BARTER, J. D., BEACH, K. L., LAKE, B. M., RUNGALDIER, H., H. R. THOMPSON, J., WANG, L., and YEE, R., 1999, What are the mechanisms for non-Bragg scattering from water wave surfaces? *Radio Sci.*, **34**, 1123–1138.
- LEWIS, B. L. and OLIN, I. D., 1980, Experimental study and theoretical model of high-resolution radar backscatter from the sea. *Radio Sci.*, **15**, 815–828.
- SLETTEN, M. A., SMITH, G. B., LIU, X., and DUNCAN, J. H., 2004, Experimental investigation of radar backscatter from plunging breakers using an ultrawideband radar and visible/infrared cameras. In *Proceedings of the 2004 International Geoscience and Remote Sensing Symposium*, September 20–24, Anchorage, Alaska, 394–397.
- SMITH, M. J., POULTER, E. M., and MCGREGOR, J. A., 1996, Doppler radar measurements of wave groups and breaking waves. *J. Geophys. Res.*, **101**, 14,269–14,282.

- TRIZNA, D. B., 1991, Statistics of low grazing angle radar sea scatter for moderate and fully developed ocean waves. *IEEE Trans. Antennas Propagat.*, **39**, 1681–1690.
- TRIZNA, D. B., 1997, A model for Brewster angle damping and multipath effects on the microwave radar sea echo at low grazing angles. *IEEE Trans. Geosci. Remote Sens.*, **35**, 1232–1244.
- WANG, P., YAO, Y., and TULIN, M. P., 1995, An efficient numerical tank for non-linear water waves, based on the multi-subdomain approach with BEM. *Int. J. Num. Meth. Fluids*, **20**, 1315–1336.
- WEST, J. C., 2000, Integral equation formulation for iterative calculation of scattering from lossy rough surfaces. *IEEE Trans. Geosci. Remote Sens.*, **38**, 1609–1615.
- WEST, J. C., 2002, LGA sea-spike backscattering from plunging breaker crests. *IEEE Trans. Geosci. Remote Sens.*, **40**, 523–526.
- WEST, J. C. and JA, S.-J., 2002, Two-scale treatment of LGA scattering from spilling breaker water waves. *Radio Sci.*, **37**, 1054, doi:10.1029/2001RS002517.
- WEST, J. C. and SLETTEN, M. A., 1997, Multipath EM scattering from breaking ocean waves at grazing incidence. *Radio Sci.*, **32**, 1455–1467.
- WEST, J. C., STURM, J. M., and JA, J.-S., 1998, Low-grazing scattering from breaking water waves using an impedance boundary MM/GTD approach. *IEEE Trans. Antennas Propagat.*, **46**, 93–100.
- WETZEL, L. B., 1986, On microwave scattering by breaking ocean waves. In *Wave Dynamics and Radio Probing of the Ocean Surface*, edited by O. M. Phillips and K. Hasselmann, (New York: Plenum Press), 273–284.
- ZHAO, Z. and WEST, J. C., 2005a, Low-grazing-angle microwave scattering from a three-dimensional spilling breaker crest: A numerical investigation. *IEEE Trans. Geosci. Remote Sens.*, **43**, 286–293.
- ZHAO, Z. and WEST, J. C., 2005b, Resistive suppression of edge effects in MLFMA scattering from finite conductivity surfaces. *IEEE Trans. Antennas Propagat.*, In press.